The Quenching Effect of BGO Crystals on Relativistic Heavy Ions in the DAMPE Experiment

Yifeng Wei, Yunlong Zhang, Zhiyong Zhang, Libo Wu, Haoting Dai, Chengming Liu, Cong Zhao, Ying Wang, Yuzhe Zhao, Peicheng Jiang, Yuanzhe Wang, F. Alemanno, M. Di Santo, E. Catanzani, Xiaolian Wang, Zizong Xu, and Guangshun Huang

***Abstract*— The DArk Matter Particle Explorer (DAMPE) is a satellite-borne, calorimetric-type, high-energy-resolution detector for the precise measurement of high-energy electrons, gamma rays, and nuclei from deep space. The DAMPE electromagnetic calorimeter consists of bismuth germanate (BGO) crystals that can measure incident hadron energies from 50 GeV to 100 TeV. For an inorganic scintillator, such as BGO, the nonlinear fluorescence response when measuring ions contributes to the difference between the experimental data and Monte Carlo simulations. This article reports the BGO quenching nonlinearity occurring in the DAMPE experiment. The ionization energy response of BGO to several kinds of ions lighter than iron is investigated by conducting beam tests and analyzing flight data. We compare the scintillator output with the energy loss according to GEANT4 simulations and determine the quenching parameters. The combined result of beam test and flight experiment shows that the quenching effect strongly depends on the density of the ionization energy loss.**

***Index Terms*— Bismuth germanate (BGO) crystal, calorimeter, DArk Matter Particle Explorer (DAMPE), heavy ions, quenching effect.**

I. Introduction

THE DArk Matter Particle Explorer (DAMPE) is a satellite-borne experiment to detect cosmic rays, including electrons, gamma rays, protons, and nuclei [1]. The experiment aims to study the origin, propagation, and acceleration of galactic cosmic rays, which attracts a lot of interest in the astrophysics community. DAMPE was launched on December 17, 2015, and has been operating at an altitude of 500 km for more than 4 years.

The bismuth germanate (BGO) calorimeter, which is composed of 308 BGO crystal bars, is the DAMPE's core subdetector. Due to the calorimeter's excellent performance for detecting electromagnetic particles, DAMPE provided the first direct observation of a 0.9-TeV break in the cosmic-ray electron plus positron spectrum [2]. The calorimeter also measures the energy of protons and nuclei (ions) from tens of GeV to approximately 100 TeV. BGO, as a typical inorganic scintillator, has a nonlinear energy response caused by the quenching effect of fluorescence photons when measuring ions. Previous studies reported this nonlinearity for light ions [3] or in lower energy ranges [4]–[6], while at a higher energy region that we are interested in, the effect has not been reported. Studies in the literature also indicated that the quenching effect depends on both the species and energies of the incident particles. In the DAMPE experiment, we considered the influence of scintillator quenching of BGO crystals to fully understand the calorimeter response to ions and the difference between the experimental data and Monte Carlo (MC) simulations.

The DAMPE detector running in orbit (called the flight model) has a backup prototype with the same design called the Engineering Qualification Model (EQM). The quenching effect is studied with relativistic heavy ions up to argon in the beam test for the EQM and with several kinds of ions in the orbit data for the flight model. Since the calorimeter response in the ion beam test, including the quenching study, has been reported in [7], in this article, we conducted the quenching study using the orbit data collected by the flight model detector and compared it with the beam test result.

II. DAMPE Instrument

Fig. 1 shows the schematic view of the DAMPE detector. It consists of four subdetectors [1], [8]: the plastic scintillator detector (PSD) serves as a charge and veto detector [9]; the silicon–tungsten tracker (STK) provides tracking [10]; the BGO calorimeter, which is the focus of this article,

Manuscript received February 14, 2020; accepted April 1, 2020. Date of publication April 24, 2020; date of current version June 19, 2020. This work was supported in part by the Joint Funds of the National Natural Science Foundation of China under Grant U1738208, Grant U1738139, and Grant U1738135, in part by the National Natural Science Foundation of China under Grant 11705197 and Grant 11673021, in part by the China Postdoctoral Science Foundation under Grant 2018M632530, in part by the Fundamental Research Funds for the Central Universities, and in part by the National Key Research and Development Program of China under Grant 2016YFA0400200.

Yifeng Wei, Yunlong Zhang, Zhiyong Zhang, Libo Wu, Haoting Dai, Chengming Liu, Cong Zhao, Ying Wang, Yuzhe Zhao, Peicheng Jiang, Yuanzhe Wang, Xiaolian Wang, Zizong Xu, and Guangshun Huang are with the State Key Laboratory of Particle Detection and Electronics, Department of Modern Physics, University of Science and Technology of China, Hefei 230026, China (e-mail: ylzhang@ustc.edu.cn; hgs@ustc.edu.cn).

F. Alemanno is with the Gran Sasso Science Institute (GSSI), 67100 L'Aquila, Italy, and also with the INFN Istituto Nazionale di Fisica Nucleare, Laboratori Nazionali del Gran Sasso, 67100 L'Aquila, Italy.

M. Di Santo is with the Dipartimento di Matematica e Fisica E. De Giorgi, Università del Salento, 73100 Lecce, Italy, and also with the Istituto Nazionale di Fisica Nucleare (INFN)—Sezione di Lecce, 73100 Lecce, Italy.

E. Catanzani is with the Dipartimento di Fisica e Geologia, Università degli Studi di Perugia, 06123 Perugia, Italy, and also with the Istituto Nazionale di Fisica Nucleare (INFN)—Sezione di Perugia, 06123 Perugia, Italy.

Color versions of one or more of the figures in this article are available online at http://ieeexplore.ieee.org.

Digital Object Identifier 10.1109/TNS.2020.2989191

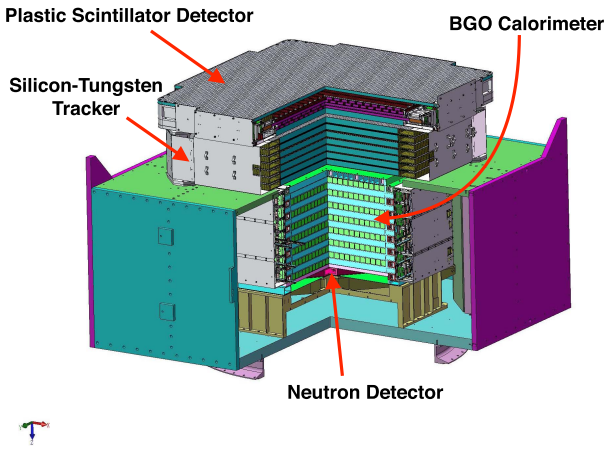

Fig. 1. Schematic of DAMPE. It is composed of a PSD, an STK, a BGO calorimeter, and an NUD.

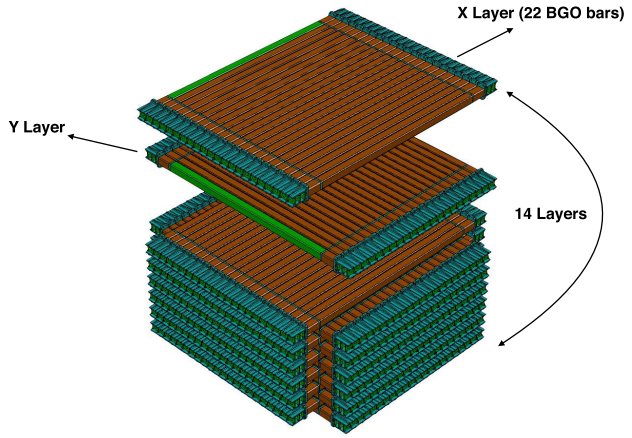

Fig. 2. Structure of the DAMPE BGO calorimeter.

provides a high precision energy measurement; and the neutron detector (NUD) improves the electron/proton discrimination power [1].

The BGO calorimeter contains 14 layers of BGO crystals (∼32 radiation lengths, ∼1.6 nuclear interaction lengths) [11]. Each layer is composed of 22 BGO crystal bars, as shown in Fig. 2. The layers alternate orthogonally in order to measure the deposited energy and the shower topology developed inside the calorimeter. The details about the readout system are reported in [12]–[14].

III. Quenching Effect in the Ion Beam Test

In this section, we briefly introduce the result obtained by measuring the quenching effect in the beam test. The test was conducted at the CERN Super Proton Synchrotron (SPS) facility in 2015. Secondary ions ranging from helium to argon with momentums of 40 and 75 GeV/n were provided in the H8 beamline. A quenching factor (ϵ) was extracted to quantitatively evaluate the quenching effect of the BGO crystals, which was defined as the ratio $E_{\mathrm{Meas}}/E_{\mathrm{MC}}$, where E_{Meas} is the measured ionizing energy deposition for the ions, which is proportional to the collected light, and E_{MC} is the theoretically deposited energy obtained from the Monte Carlo

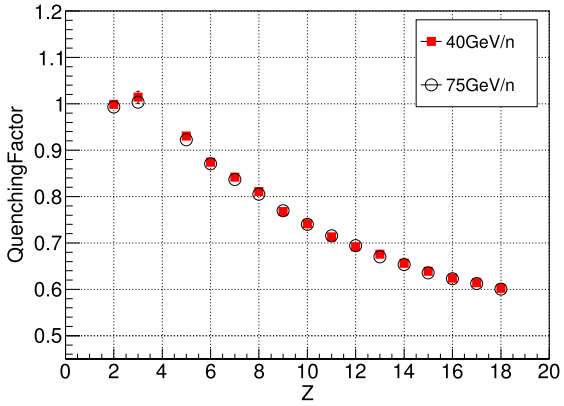

Fig. 3. Quenching factors as a function of the ion atomic number for 40 (red squares) and 75 (open circles) GeV/n beam. The error bars are statistical errors.

simulation. Fig. 3 shows the quenching factors as a function of the atomic number of the ions. It indicates that, for a given ion heavier than $Z = 5$, Birk's attenuation $(1 - \epsilon)$ increases with the atomic number. Little difference was observed between the quenching factors at 40 and 75 GeV/n. A possible explanation might be that the two sets of data are too close regarding the magnitude of the incident energy. Full details of quenching research with the beam test are reported in [7].

IV. Quenching Effect in the Flight Experiment

Since the environment in space differs from that in the ground beam test, the performance of the detector in orbit was extensively studied and then the operation and calibration methods were ascertained. The unavailability of a monoenergetic source for energy calibration has been a critical issue that is solved using the minimal ionizing particle (MIP) energy of cosmic-ray protons as the energy reconstruction benchmark. The details are presented in [8] and [15].

Incident particles in orbit, depending on the nature of cosmic rays, are more complex than that in the beam test. Generally, the cosmic-ray spectrum covers a wide energy range and is approximately subjected to a power law distribution with a spectral index of 2.7. The directions of the arriving particles are nearly isotropic because the interaction of charged cosmic rays with interstellar magnetic fields modifies their original direction [16]. Solar activities [17] and the earth's geomagnetic field [18] also affect the cosmic-ray fluxes, especially in the low-energy range.

Compared with the test beam, cosmic rays are better particle sources for studying quenching effect in a wide, continuous energy range, while some criteria should be applied in order to select high-quality events from the massive data. In this section, cosmic-ray carbon is used as an example to explain our analytical procedure, including a specific approach for studying the ions' quenching, the basic event selections for the DAMPE flight data, and the energy correction method. The procedure is described in detail below.

A. Event Selection

In this analysis, we used 3 years of flight data from January 1, 2016, to December 31, 2018. The MC data were

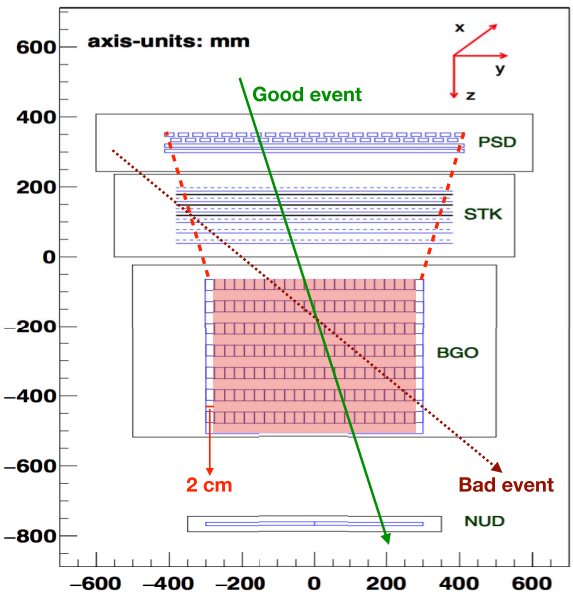

Fig. 4. Schematic of the fiducial region.

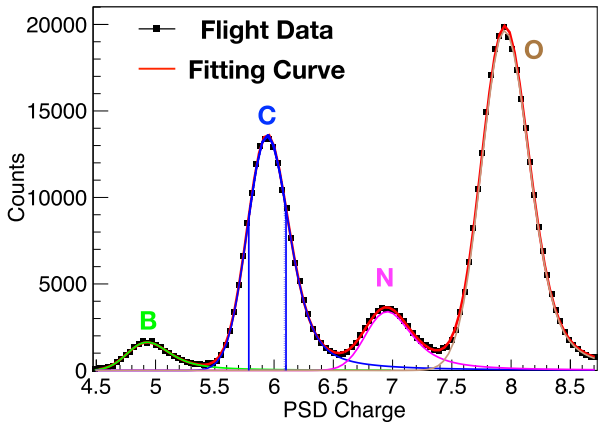

Fig. 5. Charge spectra reconstructed with the PSD, which was fit by a function of a sum of four convoluted Landau and Gaussian distributions (red line). The components for boron, carbon, nitrogen, and oxygen are green, blue, pink, and brown, respectively.

produced by the DAMPE simulation software [19], which was based on the Geant4 toolkit. The simulation data were saved in the same format as the real data so that the same analysis procedure could be applied to both data sets. The specific selection criteria are as follows.

1) *Trigger Selection:* Events had to pass the high-energy trigger (HET), which is one of the five group trigger logics of the DAMPE detector [20]. The HET is activated when a particle deposits enough energy in the calorimeter's first four layers. The ionization energy loss of ions heavier than beryllium is large enough to exceed the HET's threshold of ∼10 proton MIPs (1 MIP ≈ 23 MeV), and thus these ions activate the HET with high efficiency.
2) *Fiducial Selection:* Considering the isotropic source of charged particles in space, we only selected the events coming from the detector's acceptance angle. The fiducial selection required that: 1) a global track can be reconstructed with an associated reconstruction using the STK and BGO detectors; 2) the track had to pass through the detector from the top of the PSD to the bottom of the BGO; and 3) the position of the BGO bar for each layer's maximum energy deposition should be far away from the edge of the calorimeter (>2 cm). Fig. 4 shows the fiducial region after the selection.
3) *Charge Selection:* The PSD is responsible for the charge measurement in the DAMPE system [21], [22]. The reconstructed charges, including four kinds of ions—boron, carbon, nitrogen, and oxygen, are shown in Fig. 5. Each ion's charge spectrum is fully described using a convoluted Landau and Gaussian distribution. The total spectra were fit by the sum of the four ions' components, as marked in red in the figure. The functions for boron, carbon, nitrogen, and oxygen are green, blue, pink, and brown, respectively. The carbon selection required that the reconstructed charges were in a range of Peak(C) ± ((GSigma(C))^2 + (LWidth(C))^2)$^{1/2}$ (the blue area in Fig. 5), where GSigma(C) and LWidth(C) are the fit parameters Gaussian sigma and Landau width of the carbon component, and the Peak(C) is the charge value when the carbon's fit function reached its highest point. Since the cosmic-ray abundances showed the odd–even effect [23], the ions with even atomic numbers, such as carbon, were used as the study objects so as to reduce the contamination from their neighboring elements. The carbon contamination, which was mainly from boron, was estimated with the fit function. The specific value was less than 0.5%. Therefore, the contamination's contribution was negligible in the following analysis.
4) *MIP-E Selection:* This was crucial for the series of selections. Generally, the quenching factor was considered energy-dependent. The purpose of the selection was to determine the incident energy while studying the quenching factor. The events penetrating the entire calorimeter, without creating any shower, and the events starting shower in the beginning of the calorimeter, without providing incident ions' pure ionization energy signals, were helpless in the analysis and were abandoned by this selection.
To achieve this, we divided the calorimeter into two parts: the upper part was composed of the calorimeter's first two layers, whereas the lower part was composed of the remaining layers, as shown in Fig. 6. The selection criteria were as follows:
   a) The carbon ions had to penetrate the upper part and deposit only ionization energy. More specifically, there had to be no more than two hits in each layer of the upper part. Since the backscattering from the shower development in the lower part was inevitable, a BGO bar signal was considered a "true" hit when it was greater than a certain threshold. The threshold was 0.1 carbon MIP (1 carbon MIP ≈ 800 MeV) in this analysis.

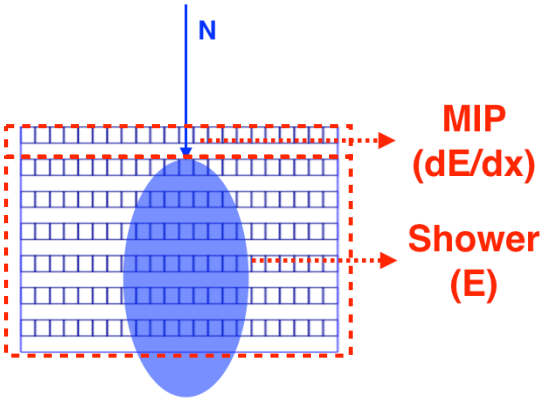

Fig. 6. Calorimeter was divided into two parts. We studied the quenching factor in the top, and measured the shower energies in the bottom.

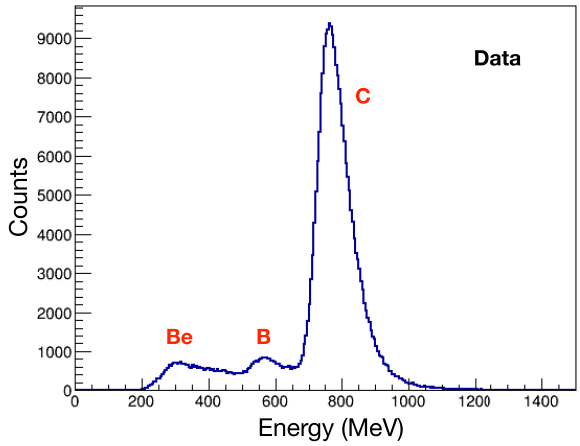

Fig. 7. Ionization energy deposition in the first layer of the BGO calorimeter after all selection applied.

b) In the lower part, the hadronic shower should develop and provide us the energy information regarding the incident ions. First, the total number of hits had to be greater than 20. The energy deposition in layer 3 or 4 had to be larger than two times of that in layer 1, to ensure that the shower started in the beginning of the lower part.

The specific kind of events passing the selection were called " MIP-E" events.

We only investigated the ionization energy loss in the calorimeter's first layer. The second layer, although used as the "upper part," played only a redundant role so that the contamination from the non-MIP events in the first layer was negligible.

The energy spectra in the first layer after selection are shown in Fig. 7. The highest peak around 800 MeV represented carbon. Two small peaks on the left of the carbon were beryllium and boron, respectively, which were identified as carbon in the PSD and then broke into lighter ion fragments in the STK or detector supporting materials between the PSD and BGO.

B. Energy Correction

Limited by the BGO calorimeter's longitudinal thickness, which was approximately 1.6 nuclear interaction lengths, some of incident energy leaked out from the bottom of the calorimeter. Meanwhile, some contributions in the hadronic shower, such as soft neutrons, neutrinos, and binding energy, could not create signals in the calorimeter. On average, ~30% of incident ions' energy was deposited inside the calorimeter with approximately 25%–35% of energy resolution. Therefore, energy correction in the analysis was essential. We used a statistical method to correct the measured energy. For a given measured energy bin i, the event number $N_{\text{meas},i}$ was expressed as the sum of the event number in all the true energy (also called incident energy) bins, $N_{\text{true},j}$, weighted by the energy response matrix

$$N_{\text{meas},i} = \sum_j M_{ij} N_{\text{true},j} \tag{1}$$

where M_{ij} is the probability that an event in the jth true energy bin is detected in the ith measured energy bin. Simulation plays a critical role in studying the calorimeter's response. An isotropic with $E^{-1.0}$ power-law spectrum was generated for the detector simulation and then is reweighted to $E^{-2.7}$ to derive energy response matrix M_{ij}, as shown in Fig. 8.

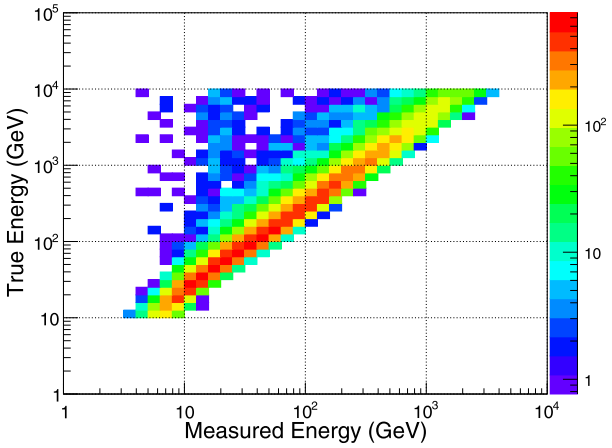

Fig. 8. Calorimeter response matrix to MC carbons.

A correction algorithm with Bayesian unfolding method [24] based on the matrix was developed to deconvolute the measured energy into true energy. Fig. 9 shows the correction result. The top panel shows ionization energy loss in the first BGO layer versus energy deposition in the calorimeter distribution for data events. A path length correction is applied to the y-axis to remove the effect of different incident angles; the unfolding correction is adopted for the x-axis to convert the measured energy into the true energy (unfolded energy). The 2-D distribution after energy unfolding is shown in Fig. 9 (bottom). The minimal y-axis value around the unfolded energy of 20 ~ 30 GeV, corresponding to the MIP, can be seen clearly after the correction. In order to more directly reflect the effect of the correction, we projected the distribution to the y-axis for each measured or unfolded energy bin in Fig. 9, yielding the 1-D ionization energy spectra, which was fit by a convoluted Landau and Gaussian distribution, as presented in Fig. 10. Fig. 11 shows the ionization energy peak value obtained from

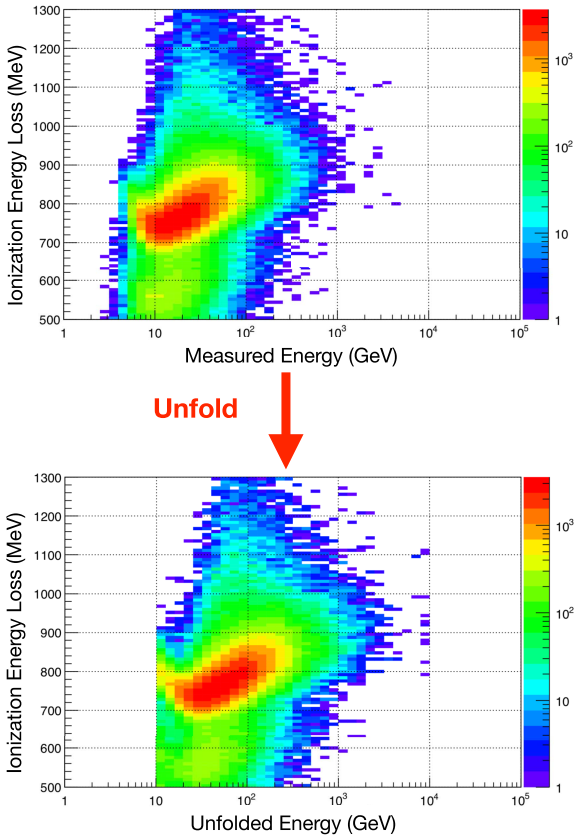

Fig. 9. Carbon ionization energy loss in the first BGO calorimeter layer versus energy deposition in BGO (top) and versus unfolded energy (bottom).

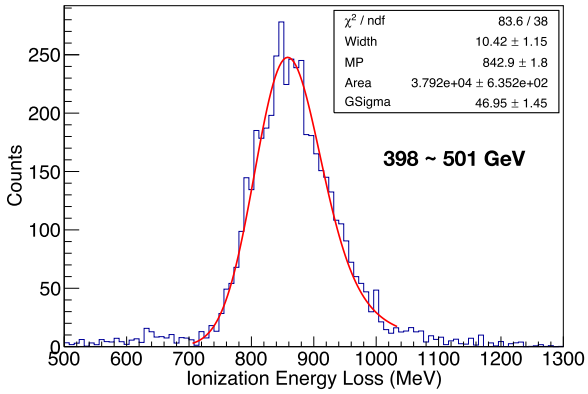

Fig. 10. Ionization energy loss of carbon in the 398–501 GeV unfolded energy bin. The spectrum is fit with a convoluted Landau and Gaussian distribution.

fitting the data as a function of energy, where the measured data (nonunfolded), unfolded data, and simulation results are shown as green, blue, and red, respectively. The unfolding method shifted the peak value to the right since the energy leakage was corrected. For the unfolded data points and simulation points, they were parallel with the same trend, following the Bethe–Bloch formula.

The systematic uncertainty caused by the unfolding correction was studied. The corrected result depends on the response matrix sensitively, which changed with the hadronic model

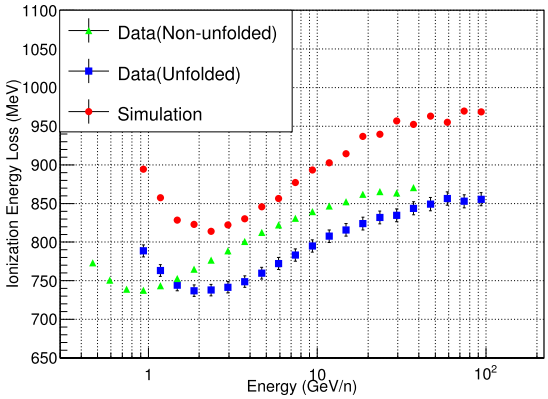

Fig. 11. Peak value of carbon ionization energy loss in the BGO as a function of the unfolded energy. The MC and flight data are shown as red and blue, respectively.

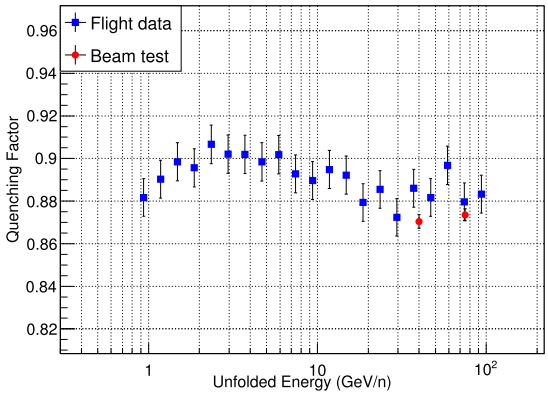

Fig. 12. BGO carbon's quenching factor as a function of the unfolded energy. The results of the flight experiment are in blue and the results of the beam test are in red.

we used in the simulation. We applied two different physics lists: QGSP_ FTFP_ BERT and FTFP_ BERT, which are considered suitable for the investigating energy range, in the Geant4 simulation to estimate the uncertainty from hadronic model. The result shows that the uncertainty is no more than 1% in all energy bins. We also ran a toy-MC simulation to generate fake observations to estimate the uncertainty from the unfolding procedure. It demonstrated that this type of uncertainty was always lower than 0.1% and was neglected.

C. Result

After the correction, the quenching factor was easily obtained. The variations in the factor in the unfolded energy of 0.83–105 GeV/n is shown in Fig. 12. The factor clearly increased and then decreased. The beam test results with energy of 40 and 75 GeV/n, as shown as red points, are also marked on this graph. The beam test results agreed with those of the flight data, in general, considering there were large fluctuations in the high-energy range due to limited statistic.

V. Discussion

In the previous section, we presented the quenching factor results of the BGO with cosmic-ray carbons in a wide energy

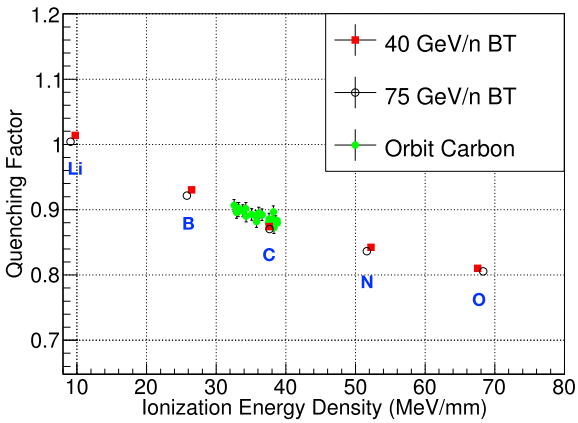

Fig. 13. Quenching factor for cosmic-ray carbon and for beam test lithium to oxygen as a function of the MC ionization energy density. The green dots, red squares, and black circle represent the cosmic-ray carbon, 40-GeV/n beam test, and 75-GeV/n beam test, respectively.

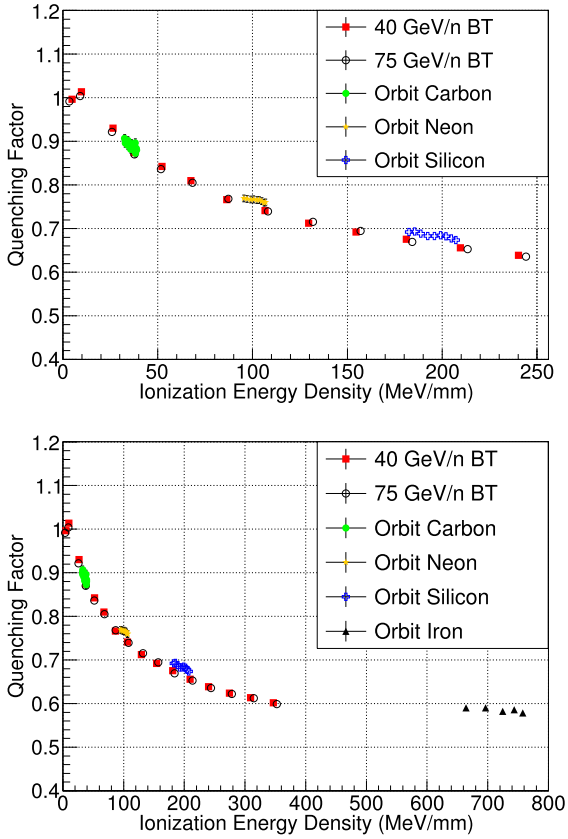

Fig. 14. Quenching factor for cosmic-ray carbon, neon, silicon, iron, and for beam test helium to argon as a function of the MC ionization energy density. The green dots, orange stars, blue crosses, black triangles, red squares, and black circles represent the cosmic-ray carbon, cosmic-ray iron, 40-GeV/n beam test, and 75-GeV/n beam test, respectively. Top: enlarged view. Bottom: complete view.

range of 1–100 GeV/n, which was consistent with the beam test results. Interestingly, by observing the variation trends in Figs. 11 and 12, we also found some anticorrelation between the quenching factor and ionization energy loss. Fig. 13 shows the quenching factor's dependence on the ionization energy loss density. The energy density was the MC energy loss normalized divided by the path length, which was the thickness of one calorimeter layer (25 mm). The figure demonstrates that the orbital carbon's quenching factor (green dots) decreased, or in other words, the quenching effect increased as the ionization energy loss in the BGO increased. To indicate a further correlation, the beam test lithium to oxygen points are also compared in the figure. The orbital carbon points are located in the connecting line of BT boron and BT carbon. We also analyzed the orbital neon, silicon, and iron data. The results including the beam test and flight data are presented in Fig. 14. It shows that the neon and silicon results were on the general trend of the beam test points, and the orbit iron points were on their extrapolation. This observational study suggested that the quenching effect depends on the density of ionization energy loss rather than the ion species. It is also noticed that the orbital neon and silicon results slightly shifted from the beam test points, which is within up to ∼3% deviation. We infer that the systematic difference may have been caused by the isotopes in the cosmic rays. However, the previous studies about neon and silicon isotopes focused on the energy range lower than 1 GeV/n [25], [26]. Further observations are necessary to obtain more accurate results.

VI. Conclusion

In [7], we have reported the BGO quenching effect to ions in the energy range of tens of GeV/n with the DAMPE beam test. In this article, we introduced a specific analysis of the DAMPE flight data and the result of measuring the BGO's quenching effect on various kinds of cosmic-ray ions above 1 GeV/n. Geant4 simulations were adopted for comparisons. The results of using cosmic rays cover a wide relativistic energy range, for instance, two orders of magnitude for carbon, which was not reported in previous studies. Considering the energy and ion species, we established a joint observation with beam test and flight experiment. The result shows that the quenching factors of ions with different energies were on the same varying curve, which may indicate that the quenching effect mainly depends on the ionization energy density.

References

[1] J. Chang *et al.*, "The dark matter particle explorer mission," *Astroparticle Phys.*, vol. 95, pp. 6–24, Oct. 2017.
[2] D. Collaboration, "Direct detection of a break in the teraelectronvolt cosmic-ray spectrum of electrons and positrons," *Nature*, vol. 552, no. 7683, pp. 63–66, Dec. 2017.
[3] V. V. Avdeichikov *et al.*, "Light output and energy resolution of CsI, YAG, GSO, BGO and LSO scintillators for light ions," *Nucl. Instrum. Methods Phys. Res. A, Accel. Spectrom. Detect. Assoc. Equip.*, vol. 349, no. 1, pp. 216–224, Sep. 1994.
[4] E. Valtonen, J. Peltonen, and J. J. Torsti, "Response of BGO and CsI (TI) scintillators to heavy ions," *Nucl. Instrum. Methods Phys. Res. A, Accel. Spectrom. Detect. Assoc. Equip.*, vol. 286, nos. 1–2, pp. 169–174, 1990.
[5] Z. Dlouhý *et al.*, "The response of BGO scintillation detectors to light charged nuclei," *Nucl. Instrum. Methods Phys. Res. A, Accel. Spectrom. Detect. Assoc. Equip.*, vol. 317, no. 3, pp. 604–606, Jul. 1992.
[6] J. Tammen, R. Elftmann, S. R. Kulkarni, S. I. Böttcher, and R. F. Wimmer-Schweingruber, "Quenching comparison of BGO and BSO for heavy ions," *Nucl. Instrum. Methods Phys. Res. B, Beam Interact. Mater. At.*, vol. 360, pp. 129–138, Oct. 2015.
[7] Y. Wei *et al.*, "Performance of the DAMPE BGO calorimeter on the ion beam test," *Nucl. Instrum. Methods Phys. Res. A, Accel. Spectrom. Detect. Assoc. Equip.*, vol. 922, pp. 177–184, Apr. 2019.

[8] G. Ambrosi *et al.*, "The on-orbit calibration of dark matter particle explorer," *Astroparticle Phys.*, vol. 106, pp. 18–34, Nov. 2019.
[9] Y. Yu *et al.*, "The plastic scintillator detector for DAMPE," *Astroparticle Phys.*, vol. 94, pp. 1–10, Sep. 2017.
[10] P. Azzarello *et al.*, "The DAMPE silicon–tungsten tracker," *Nucl. Instrum. Methods Phys. Res. A, Accel. Spectrom. Detect. Assoc. Equip.*, vol. 831, pp. 378–384, Sep. 2016.
[11] Y. Wei *et al.*, "Performance of the BGO detector element of the DAMPE calorimeter," *IEEE Trans. Nucl. Sci.*, vol. 63, no. 2, pp. 548–551, Apr. 2016.
[12] Z. Zhang *et al.*, "Design of a high dynamic range photomultiplier base board for the BGO ECAL of DAMPE," *Nucl. Instrum. Methods Phys. Res. A, Accel. Spectrom. Detect. Assoc. Equip.*, vol. 780, pp. 21–26, Apr. 2015.
[13] Y.-L. Zhang *et al.*, "A high dynamic range readout unit for a calorimeter," *Chin. Phys. C*, vol. 36, no. 1, pp. 71–73, Jan. 2012.
[14] C. Feng *et al.*, "Design of the readout electronics for the BGO calorimeter of DAMPE mission," *IEEE Trans. Nucl. Sci.*, vol. 62, no. 6, pp. 3117–3125, Dec. 2015.
[15] L. Wu *et al.*, "Calibration and status of the 3-D imaging calorimeter of DAMPE for cosmic ray physics on orbit," *IEEE Trans. Nucl. Sci.*, vol. 65, no. 8, pp. 2007–2012, Aug. 2018.
[16] J. R. Jokipii, "Cosmic-ray propagation. I. charged particles in a random magnetic field," *Astrophys. J.*, vol. 146, p. 480, Nov. 1966.
[17] M. Potgieter, "Solar modulation of cosmic rays," *Living Rev. Sol. Phys.*, vol. 10, no. 1, p. 3, 2013.
[18] W. R. Webber and F. B. McDonald, "Cerenkov scintillation ounter measurements of the intensity and modulation of low rigidity cosmic rays and features of the geomagnetic cutoff rigidity," *J. Geophys. Res.*, vol. 69, no. 15, pp. 3097–3114, Aug. 1964.
[19] C. Wang *et al.*, "Offline software for the DAMPE experiment," *Chin. Phys. C*, vol. 41, no. 10, Oct. 2017, Art. no. 106201.
[20] Y.-Q. Zhang *et al.*, "Design and on-orbit status of the trigger system for the DAMPE mission," *Res. Astron. Astrophys.*, vol. 19, no. 9, p. 123, Sep. 2019.
[21] M. Ding *et al.*, "Calibration of the DAMPE plastic scintillator detector and its on-orbit performance," *Res. Astron. Astrophys.*, vol. 19, no. 3, p. 047, Mar. 2019.
[22] T. Dong *et al.*, "Charge measurement of cosmic ray nuclei with the plastic scintillator detector of DAMPE," *Astroparticle Phys.*, vol. 105, pp. 31–36, Feb. 2019.
[23] T. K. Gaisser, R. Engel, and E. Resconi, *Cosmic Rays and Particle Physics*. Cambridge, U.K.: Cambridge Univ. Press, 2016.
[24] G. D'Agostini, "A multidimensional unfolding method based on bayes' theorem," *Nucl. Instrum. Methods Phys. Res. A, Accel. Spectrom. Detect. Assoc. Equip.*, vol. 362, nos. 2–3, pp. 487–498, Aug. 1995.
[25] R. A. Mewaldt, J. D. Spalding, E. C. Stone, and R. E. Vogt, "High resolution measurements of galactic cosmic-ray neon, magnesium, and silicon isotopes," *Astrophysical J.*, vol. 235, pp. L95–L99, Jan. 1980.
[26] A. Lukasiak, P. Ferrando, F. B. McDonald, and W. R. Webber, "Cosmic-ray isotopic composition of C, N, O, Ne, Mg, SI nuclei in the energy range 50-200 MeV per nucleon measured by the voyager spacecraft during the solar minimum period," *Astrophys. J.*, vol. 426, pp. 366–372, May 1994.